Applied Physics A (2023) 129:99
https://doi.org/10.1007/s00339-023-06386-7

Applied Physics A
Materials Science & Processing

Tunable and light-weight phononic lattices inspired by spider capture silk

Chao Ma[1] · Shiheng Zhao[1] · Jianbo Zhang[1] · Zheng Chang[1]

Received: 14 September 2022 / Accepted: 4 January 2023

Abstract
Inspired by the morphology and material composition of spider capture silk, we report a one-dimensional (1D) bead-chain phononic lattice (BCPL) that is lightweight and possesses tunable bandgaps. Among the mechanical parameters of the stress-free structure, we demonstrate that the width and midfrequency of the bandgaps depend mainly on the shear modulus and the mass density of the beads, while the axial pre-stretching exhibits a flexible and appreciable bandgap tunability. Based on this, mimicking the local morphology of the orb-web, we subsequently propose a two-dimensional (2D) BCPL with the 1D BCPL as components. Numerical simulations verify its wave filtering and directional transmission capabilities, which are regulated by tensile deformation. This work is expected to shed some light on the design and development of lightweight tunable elastic wave modulation devices.

Keywords Phononic crystal · Bandgap · Bioinspired · Spider web · Capture silk · Prestress

1 Introduction

Phononic crystals (PCs) [1–3] have aroused considerable research interest due to their ability to tailor the propagation of acoustic/elastic waves, and particular attention has been paid to PC bandgaps, i.e., the range of frequencies where waves are prohibited. Efforts have been made to modulate the PC bandgap properties (e.g., bandwidth and midfrequency), which facilitate a wide range of applications, including waveguiding [4, 5], energy harvesting [6, 7], and vibration isolation [8, 9].

The bandgaps of PCs depend on their formation mechanisms [1, 10, 11] and are closely related to the structural and material compositions of primitive cells. Ever since PCs were proposed, various structural configurations [12, 13] and material combinations [14, 15] have been consistently explored for the dedicated design of bandgap frequencies or to broaden the bandgaps. Recently, architected lattice structures [16–19] have opened an avenue for lightweight phononic lattices (PLs). The spatially periodic networks of structural elements (e.g., beams, bars, and shells) yield high porosity with novel wave phenomena [12, 19–22] not found in conventional PCs. In addition to weight efficiency, the designed structure also demands bandgap tunability to accommodate multiple working scenarios and requirements. A feasible solution involves applying mechanical stimuli [15, 23–27], which change the PL's effective material properties and sometimes the geometry configuration in a reversible manner without additional requirements for the material composition (e.g., without thermal, magnetic, or electrical responses). In particular, the PLs with soft (i.e., highly deformable) phases [25, 28] have demonstrated robustness in modulating bandgaps with finite pre-deformation.

However, many biomaterials and structures in nature, such as the spider webs [29–33], honeycomb [34], stem tissue of aquatic plants [35], and cochlea [36] have been of great interest due to their remarkable elastodynamic performance. An orb-web is a mechanically stable construction with a prestressed frame and threads (radial and capture silk) that appears to be extraordinarily weight-efficient and stable at different scales [37]. Notably, the periodic arrangement of vertically intersecting radial and capture silks facilitates directional signal transmission and makes the orb-web serve as an "eye" for a spider to perceive the external environment accurately [38, 39]. Additionally, the capture silk renders

Chao Ma and Shiheng Zhao have contributed equally to the study.

✉ Zheng Chang
changzh@cau.edu.cn

[1] College of Science, China Agricultural University, Beijing 100083, China

Published online: 11 January 2023

a unique periodic bead-chain appearance consisting of a thread with uniformly distributed glue droplets [40–42] (Fig. 1a). The elastic modulus of the chain is about 10 to 100 times larger than that of the bead, whereas the densities of the two components are of the same order [43]. This type of material and structural configuration strongly suggests that the capture silk and the orb-web made of this substance are natural PLs that contribute to hindering the circumferential propagation of elastic waves in the web.

For such ideal bionic design exemplars, morphological mimicry is straightforward, whereas revealing the mechanisms behind their dynamical properties requires careful analysis. On the one hand, in terms of the droplet and silk's material, they exhibit different compositions from conventional 1D PL that designing the desired bandgaps usually requires the introduction of materials with high relative density and modulus as a resonant unit or scatterer [14, 44–47]. Thus, exploring the unique material composition (similar low densities and vastly different moduli) is essential for understanding their biological function and guiding the design of related structures. On the other hand, the prestress distributed in the silk is generally considered to maintain structural stability. However, when these silks are regarded as a PL, the effect of prestress on its elastodynamic characteristics, especially the wave propagation character, such as bandgap, needs to be further clarified. As the goal of this paper to address, we summarize the following issues: what do the material and structural properties contribute to the capture silk and orb-web's wave propagation? How does prestressing affect these highly deformable structures and thus elastic wave propagation?

To clarify the questions, in this study, we construct a 1D bead-chain phononic lattice (BCPL) inspired by spider capture silk and explore its elastic wave propagation through numerical simulations. The influence of the mechanical properties of the bead and chain on the band structure is carefully analyzed for the specific structural configuration, which demonstrates that the BCPL's bandgap properties are dominated by the bead's density and shear modulus. Based on the Small-on-Large theory [48], we also show that finite prestress can modulate the band structure and broaden the bandgaps. In addition to this, we propose a 2D BCPL with the 1D BCPL as a critical component by imitating the orb-web's local morphology. Numerical simulations illustrate that the prestress is a robust mechanism for switching the bandgaps on and off and tuning features such as wave-filtering and directional transmission on demand.

The rest of this paper is arranged as follows. The model description of the BCPLs and the method for the numerical simulations are presented in Sects. 2, 3, respectively. The band structures of the 1D and 2D BCPLs and the influence of the material parameters and pre-stretching on them are analyzed and discussed in Sect. 4. The concluding remarks are discussed in Sect. 5.

2 Model description

2.1 The one-dimensional bead-chain phononic lattice

We exploit the essential structural characteristics of typical spider capture silk (Fig. 1a) and consider a 1D BCPL consisting of uniformly distributed "beads" strung together with a "chain," in which the term "1D" refers to both the unidirectional periodicity and the unidirectional elastic wave propagation of the BCPL. We take the 2D planar geometry (Fig. 1c) of the silk and focus on the wave propagation with the plane-strain assumption. This means that the model corresponds to a thin-walled phononic plate [49] that extends infinitely along the out-of-plane direction. In contrast, for a 3D bead-chain phononic structure with an out-of-plane scale much smaller than its length, the wave propagation can be described by an identical 2D model, but with the assumption of plane-stress. In this context, the research method described in this work is also applicable provided that a material parameter substitution is performed to obtain the plane-stress solution from the plane-strain problem [50].

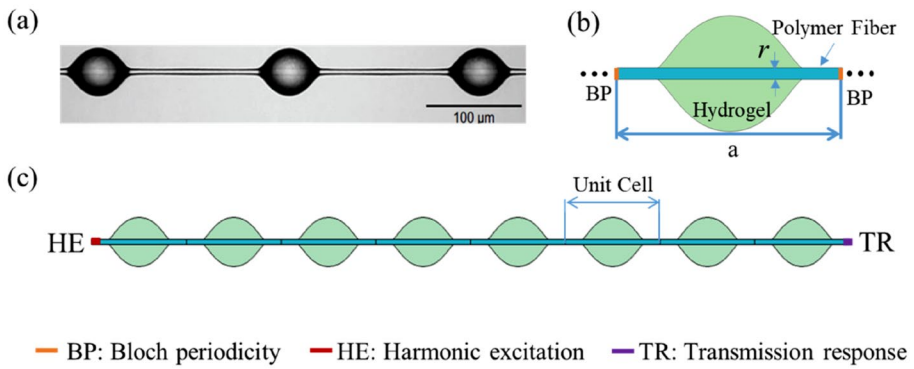

Fig. 1 Schematic diagrams of the 1D BCPL. **a** A photomicrograph of spider capture silk. **b** and **c** are the primitive cell and the supercell of the 1D BCPL. The boundary conditions applied in order to calculate the band structure and transmission spectrum of the 1D BCPL are labeled in **b** and **c**, respectively

Here we only consider the longitudinal and transverse modes and ignore the torsional mode because the former two, compared to the latter, are more convenient and thus more widely utilized in applications such as nondestructive testing [51].

The primitive cell of the 1D BCPL is shown in Fig. 1b. Referencing real silk, the width and length of the "chain" are $r = 1.3\ \mu m$ and $a = 25\ \mu m$, while the bead is considered an oval depicted by a sequence of cubic Bézier curves. Among the various engineering materials that exhibit similar mechanical properties to the silk components, we select melt-processible rubber as the chain [52], while hydrogel with a similar density but a significantly different modulus [53] is selected as the bead. Therefore, the (initial, or linear) Lamé constants and mass densities of bead and chain are set to be $\lambda_{0b} = 0.29$ MPa, $\mu_{0b} = 0.07$ MPa, and $\rho_{0b} = 1.06$ g /cm^3, and $\lambda_{0c} = 4.29$ MPa, $\mu_{0c} = 1.07$ MPa, and $\rho_{0c} = 1.2$ g /cm^3, respectively. Among various hyperelastic models, the 2D variant of the compressible Arruda–Boyce strain energy function [54],

$$W = C_1\left[\frac{1}{2}(I_1-2)+\frac{1}{20N}(I_1^2-4)+\frac{11}{1050N^2}(I_1^3-8)+\frac{19}{7000N^3}(I_1^4-16)+\frac{519}{673750N^4}(I_1^5-32)\right]-\mu\ln(J)+\frac{\lambda}{2}(J-1)^2 \tag{1}$$

is utilized for which it demonstrates superiority in describing the mechanical behavior of rubber [55] and hydrogel [56]. In Eq. (1), $C_1 = \mu/\left(1+2/5N+44/175N^2+152/875N^3+834/67375N^4\right)$ is derived according to the rules [57] of $W(\mathbf{F}=\mathbf{I})=0$, $\partial W(\mathbf{F}=\mathbf{I})/\partial\mathbf{F}=0$ and $\partial^2 W(\mathbf{F}=\mathbf{I})/\partial\mathbf{F}\partial\mathbf{F} = \lambda\delta_{ij}\delta_{kl}+\mu\delta_{ik}\delta_{jl}+\mu\delta_{il}\delta_{jk}$. I_1 is the first invariant of the right Cauchy–Green tensor and J is the volumetric ratio. N is a material constant denoting a measure of the limiting network stretch, and we set $N = 5$ for both chain and bead as it provides a good fit to the existing experiments [58] on rubbery materials. In this model, the viscosity of the material is not considered since several works [15, 59] have demonstrated that material loss will not cause a qualitative change in the band structure, but some slight band shifts in a soft system with high porosity but some slight band shifts.

2.2 The two-dimensional bead-chain phononic lattice

An orb-web is mainly composed of radially distributed threads without any "beads" on them and a capture-spiral approximately perpendicular to them, thus forming an axisymmetric structure with local orthogonality and circumferential periodicity (Fig. 2a). In addition, radial silk is thicker and stiffer than capture silk for the structural support and directional transmission of wave signals. The 2D BCPL considered in this work imitates the web's local morphology

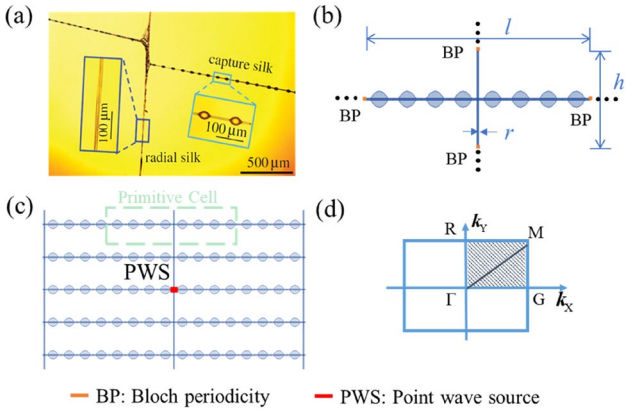

Fig. 2 Schematic diagrams of the 2D BCPL. **a** A magnified view of the local morphology of a typical orb-web [41]. **b** and **c** are the primitive cell and supercell of the 2D BCPL. **d** is the first irreducible Brillouin zone of the primitive cell. The boundary conditions applied in order to calculate the band structure and wavefield of the 2D BCPL are labeled in **b** and **c**, respectively

but ignores the structure's radial gradient and presents a rectangular lattice (Fig. 2c) with periodicity in both orthogonal directions. Additionally, to make the wave behaviors in the two principal directions similar, we utilize the 1D BCPLs as the horizontal components and those without beads as the vertical counterparts.

The primitive cell of the 2D BCPL is shown in Fig. 2b. With the length and the width set to be $l = 8a$ and $h = 2a$, respectively, the geometric and material parameters of the local components are identical to those of the 1D BCPL.

3 Methods for numerical simulations

The wave propagation behaviors of both BCPLs are simulated with COMSOL Multiphysics.

3.1 The band structure and the transmission spectra of the 1D BCPL

The band structure of the 1D BCPL is obtained using the eigenfrequency analysis of the solid mechanics module, with the Floquet–Bloch boundary conditions being imposed at the left and right boundaries of the primitive cell (Fig. 1b). The primitive cell is discretized by a triangular mesh with a quadratic displacement shape function, and the mesh quality (characterized by the skewness) is guaranteed to be above 0.6. Given the wavenumber $k_x \in [0,\ \pi/a]$ in the $\Gamma - G$ direction, twelve eigenvalues are calculated for the band structure in the frequency range of [0, 0.9] MHz. To distinguish the propagation modes, the polarization factor [60] is defined as $p = \int u_1^2 ds / \int (u_1^2 + u_2^2) ds$, in which the integral

takes over the unit cell, and u_1 and u_2 are the displacements along the x-direction and the y-direction, respectively. is the area element. In this fashion, $p = 1$ and $p = 0$ correspond to the P- (longitudinal) and S- (transverse) modes, respectively, while the other cases correspond to the coupled modes.

A parametric sweep is performed in the numerical simulations of the 1D BCPL to explore the influence of the material parameters on the band structure, with the Lamé constants of the chain and bead (λ_c, μ_c, λ_b, and μ_b) defined to be $\gamma \in [1,\ 100]$ times larger than that of initially provided, and the mass densities of the chain and bead (ρ_c and ρ_b) set to be in the range of $\rho \in [0.248,\ 5]\ \mathrm{g}/\mathrm{cm}^3$ and to vary linearly with γ. We sweep one or two of the six material parameters in one simulation and keep the rest as initial values. Subsequently, the bandwidths and mid-frequencies of the complete and incomplete bandgaps are extracted to analyze their evolution with different parameters.

The transmission spectra are calculated with the same module utilized for a supercell with eight primitive cells in frequency domain analysis, as shown in Fig. 1c. The left boundary of the supercell is set to be a wave source that generates harmonic elastic waves of the P-modes, S-modes, or coupled modes. The right boundary of the supercell is set to be an output terminal. The transmission coefficient is defined as $T = 20\lg\left(u_{\mathrm{out}}/u_{\mathrm{in}}\right)$, with u_{in} and u_{out} being the integrated total displacements on the input and the output terminals, respectively. The transmission spectra are calculated with the wave source frequency of [0, 0.9] MHz.

3.2 The band structure and the steady-state wavefield of the 2D BCPL

The simulation setup for the band structure of the 2D BCPL is the same as that of the 1D BCPL, except that we impose Floquet–Bloch boundary conditions around the primitive cell to obtain the dispersion relationship at all the edges of the first irreducible Brillouin zone (Fig. 2d) with the path $\Gamma - \mathrm{G} - \mathrm{M} - \mathrm{R} - \Gamma$. With the corresponding wavenumber in the path, 100 eigenfrequencies are searched and the band structures are plotted in [0.2, 0.4] MHz.

Correspondingly, the steady-state wave field in a 2D BCPL consisting of 9×3 primitive cells is calculated in the frequency domain. In the simulation, we apply fixed constraints on the periphery of the finite structure. A point wave source (Fig. 2c) is imposed at the center to generate P-, S- or coupled wave modes, which is achieved by specifying the displacement components of a tiny circumference, i.e., $u_1 = A\cos(\omega t)$, $u_2 = A\sin(\omega t)$ for the P-wave and $u_1 = -A\sin(\omega t)$, $u_2 = A\cos(\omega t)$ for the S-wave. Given the excitation amplitude of $A = 0.02\ \mu m$ at the corresponding frequency, the steady-state displacement field distribution is obtained and multiplied by the amplification factor of 300 to obtain intuitive results.

3.3 Elastic wave behavior of pre-stretched BCPLs

We employ the Small-on-Large theory to analyze the linear elastic wave propagation in finitely stretched BCPLs. In the theory, a finitely pre-deformed hyperelastic medium is considered to be a stress-free effective medium, while it is assumed that the small-amplitude wave motion does not affect the effective properties. Specifically, for a hyperelastic material with the strain energy density, W the effective material parameters after deformation can be expressed as [48]

$$\tilde{C}_{0IjKl} = J^{-1}F_{Ii}F_{Kk}C_{ijkl},\ \ \tilde{\rho} = J^{-1}\rho_0, \tag{2}$$

where $C_{ijkl} = \partial W / \partial F_{ji}\partial F_{lk}$ and ρ_0 represent the initial elastic tensor and the density, and F_{ij} and $J = \det(F_{ij})$ represent the deformation gradient and its determinate, respectively.

A two-step model [50, 54] is utilized in the numerical simulations based on the above theory. First, the finite deformation of a primitive cell of the BCPLs is calculated using the nonlinear quasi-static analysis with the solid-mechanics module. Second, with the deformed geometry and the deformation gradient that are obtained in the first step being imported, the band structures, transmission spectra, or steady-state wavefields of the BCPLs are determined by using the weak-form PDE module with the corresponding boundary conditions.

4 Results and discussion

4.1 Complete and incomplete bandgaps of the 1D BCPL

Figure 3a displays the band structure of the 1D BCPL with the initial material parameters and without the pre-stretch in the frequency [0, 0.9] MHz. The polarization distinguishes the propagation modes of different branches, allowing the identification of incomplete and complete bandgaps. It is shown that there are three P-wave incomplete bandgaps (IBGs,[0.3462, 0.6199] MHz , [0.6332, 0.6757] MHz , and [0.7826, 0.8125] MHz) and three S-wave incomplete bandgaps ([0.036, 0.0471] MHz, [0.1277, 0.3462] MHz, [0.7195, 0.7599] MHz) in the frequencies of interest. Correspondingly, two complete bandgaps (CBGs, [0.4383, 0.5311] MHz and [0.7599, 0.78312] MHz) can be observed in the overlapping region of the two types of IBGs.

Figure 3b–d displays the transmission spectra for the P-, S-, and coupled harmonic waves propagating through

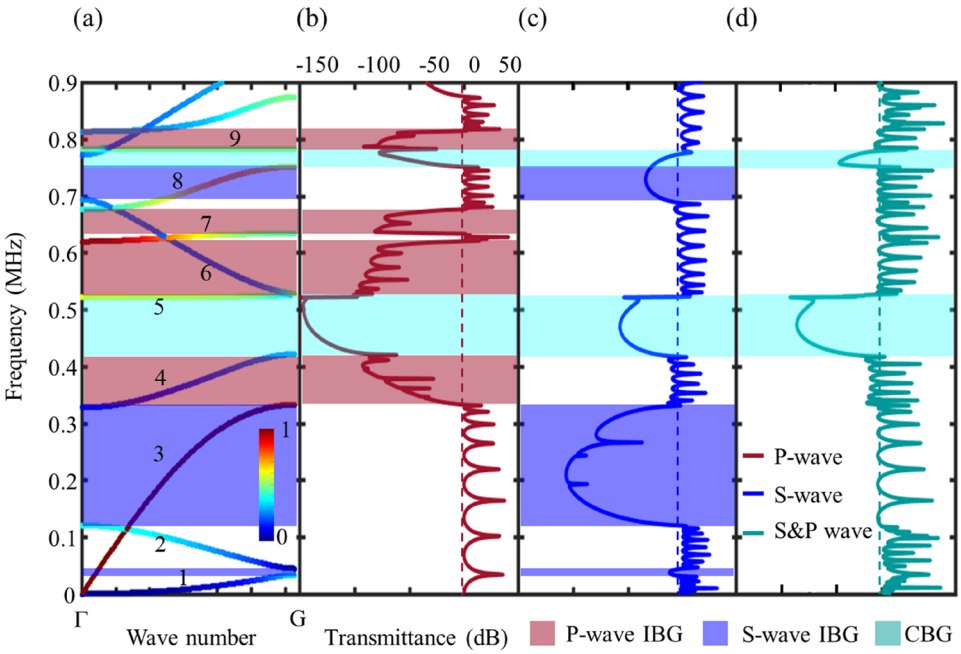

Fig. 3 Band structure and transmission spectra of the 1D BCPL. **a** The band structure of the BCPL with initial material parameters and without any pre-stretch. The polarization distinguishes the propagation modes corresponding to the different branches along the *x*-axis. The red and blue colors indicate the P-mode and S-mode, respectively, whereas the other colors indicate the coupled modes. **b–d** Transmission spectra for P-, S-, and coupled harmonic wave sources. In **a–d**, the IBGs for the P-wave and the S-wave are shaded in red and blue, respectively, while the CBGs are shaded in cyan

the 1D BCPL, showing good agreement with the bandgaps annotated in the band structure while exhibiting an excellent vibration isolation capability for the BCPL.

4.2 Effects of material parameters on the 1D BCPL

The opening, closing, and shifting of the bandgaps are determined by the shifting and overlapping of the dispersion curves in the band structure. Figure 4 shows the effect of the material parameters (λ_c, μ_c, ρ_c, λ_b, μ_b, and ρ_b) on the lowest CBG, first P-wave IBG, and second S-wave IBG (see Fig. 3a) of the 1D BCPL. As can be observed in Fig. 4a, d, both the midfrequency and the width of the lowest CBG are significantly affected by μ_c, ρ_c, and ρ_b. As μ_c increases, both the midfrequency and the bandgap width increase monotonically. In contrast, the midfrequency decreases monotonically as ρ_c and ρ_b increase, whereas the bandgap width increases and then decreases, with the maximum values exhibited in these cases. Figure 4b, c, e and f shows that μ_c has a similar effect for the IBGs. However, the effects of ρ_c and ρ_b exhibit a clear difference. An increase in ρ_b lowers the midfrequency and bandgap width of the P-wave IBG as well as the midfrequency of the S-wave IBG. In contrast, a variation in ρ_c has little effect on the IBGs.

Since μ_b has the most significant effect on the bandgaps, its effect on more bandgaps is further shown in Fig. 5a. As μ_b increases, in addition to the continuously broadening first CBG, a second CBG exists for $\mu_b > 1.2$ MPa, which greatly broadens the bandgap width in the frequency of interest.

Above results help us to speculate spider's wisdom on efficiency. For spiders, the low density of the silk and droplet makes their preparation easier. Due to the relatively low shear modulus of the beads, in which case the spider cleverly uses the smallest possible density to compensate for this deficiency (Fig. 4a, d, initial density where locates near the cross of the two blue lines), and results in a broader bandgap width. Similarly, as can be seen in Figs. 4d, e, the first-two bandgap widths are the largest at smaller densities. However, it should be noted that an increase in shear modulus increases both the width and midfrequency of the bandgap, so a low frequency and sufficiently wide bandgap requires an elaborate design of shear modulus.

For the bionic design, the common engineering materials that can be found in the material parameter space are displayed in Fig. 5b, providing a correspondence between the bandgap properties and the material implementation. It is suggested that the position of the bandgap can be adjusted via the material selection of the bead component, while the bandgap is kept at a broad level.

4.3 Effect of the pre-stretching on the 1D BCPL

To explore the pre-stretching on the band structure of the 1D BCPL, the primitive cell is applied with a specified displacement of the rightward direction on its right boundary, with the left boundary constrained with a roller and the other boundaries kept free. In this deformation state, an inhomogeneous distribution of the deformation is presented in the primitive cell, as shown in an example in Fig. 6a with the deformation gradient F_{11}.

Following the method provided in Sect. 3.3, the band structures for the nominal strain (the elongation of the

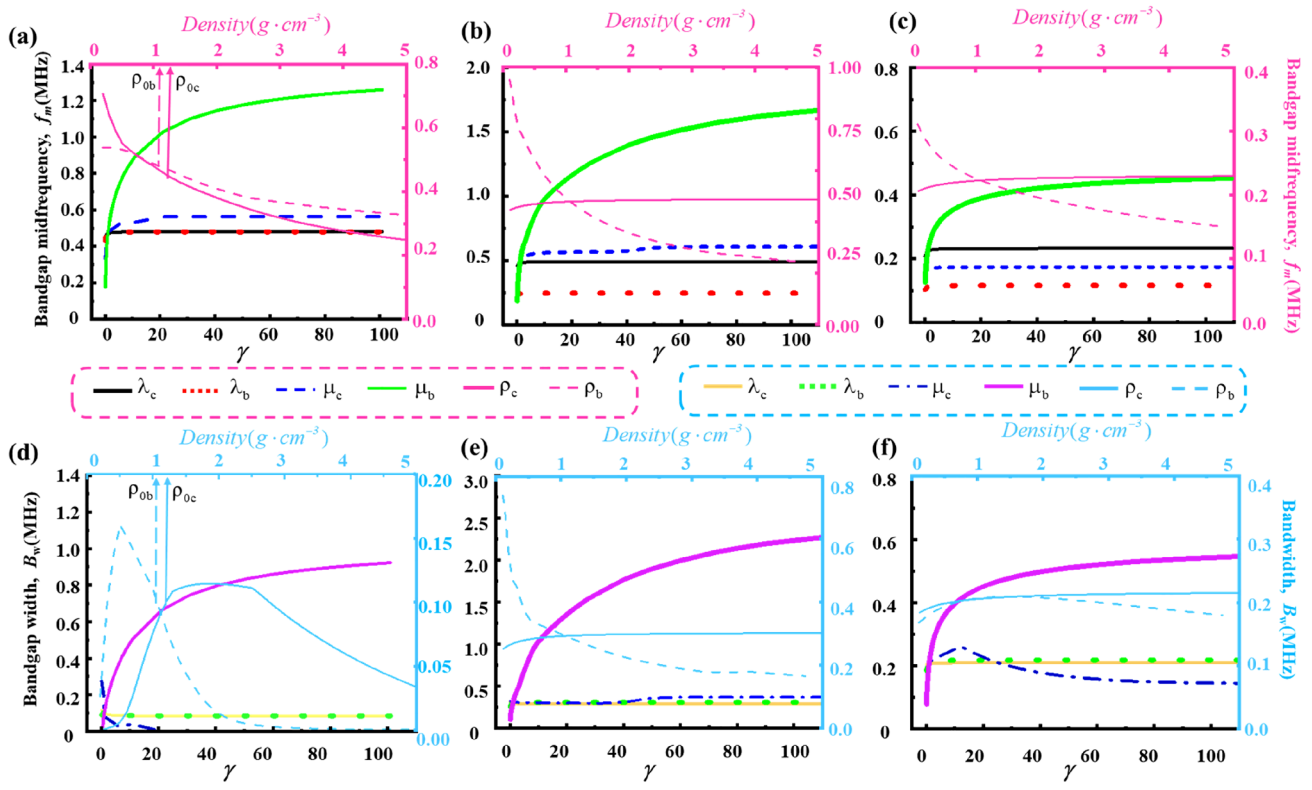

Fig. 4 Influence of material parameters on CBG and the IBGs of the 1D BCPL. **a**, **d**, **b**, **e**, and **c**, **f** are the bandgap midfrequency and bandgap width of the lowest CBG and the lowest IBGs for the P-wave and S-wave. The initial values of bead and chain's density (ρ_{0b}, ρ_{0c}) are marked by arrows in **a** and **b**, while the initial moduli are corresponding to $\gamma = 1$

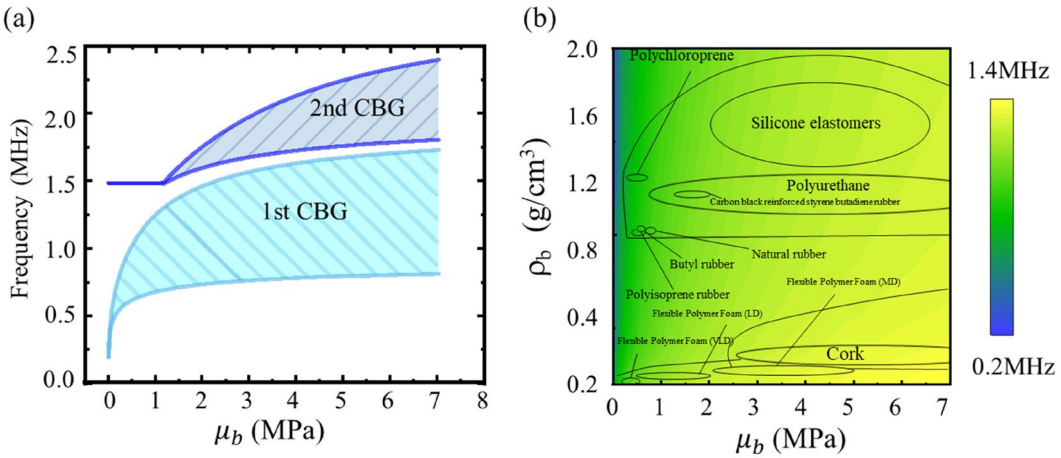

Fig. 5 **a** Influence of μ_b on the first and second CBGs. **b** the color map of the mid-frequency of the first CBG. The common engineering materials corresponding to the material parameter space are displayed in (**b**)

chain divided by its original length) $\varepsilon = 0.1,\ 0.2,\ 0.3$ can be obtained, as shown in Fig. 6b–d. The figure clearly exhibits that the bandgap evolution is governed by the frequency shift of branches of different propagation modes. Meanwhile, a frequency shift pattern in that the P-polarized branches generally move to lower frequencies, whereas the S-counterparts move upward more significantly can be observed. The mechanism for the frequency shifts of different branches can be explained [50] by the competition between changes in the geometry configuration (mainly the current length of the primitive cell) and that in the effective material parameters (i.e., the instantaneous Young's modulus and shear modulus

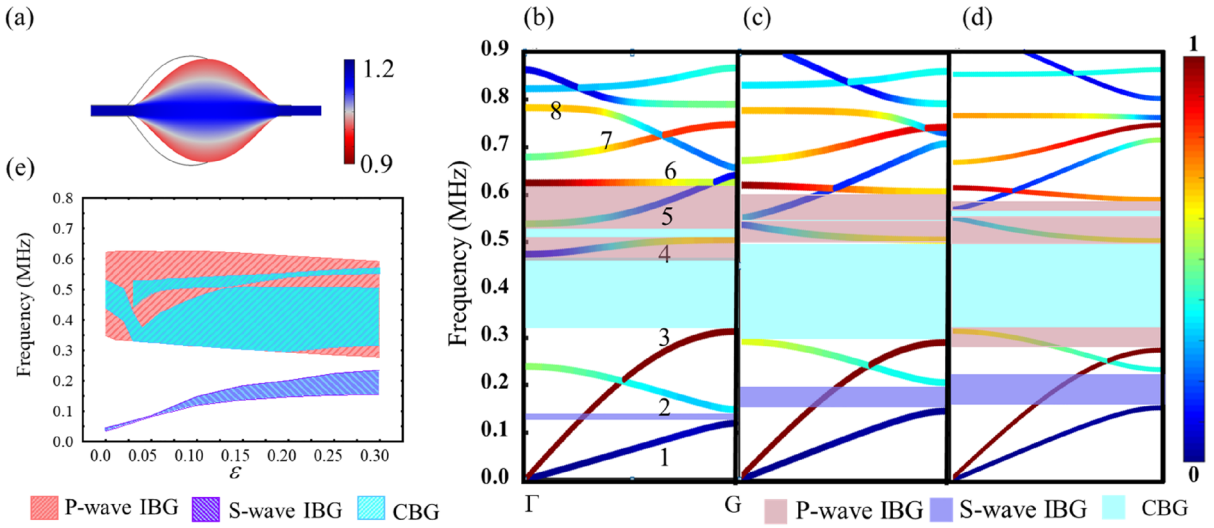

Fig. 6 Band structures of the pre-stretched 1D BCPL. **a** Deformation state and the corresponding distribution of the deformation gradient F_{11} of the 1D BCPL with pre-stretching. **b–d** are the band structures for the nominal strains $\varepsilon = 0.1$, 0.2, and 0.3. The color of the branches represents the dimensionless polarization as described in Fig. 3. **e** The evolution of the first P-wave IBGs, S-wave IBGs, and CBGs with the increase of the pre-stretching

of the structure): the increase in the length of the structure shifts both modes toward lower frequencies. Conversely, an increase in the effective material parameters shifts the frequencies of the two modes upward in diverse degrees. Typically, the increase in the effective Young's modulus (which determines the frequencies of the P-modes) is smaller than that of the effective shear modulus (which governs the frequencies of the S-modes) for the same degree of stretching, resulting in the above frequency shift pattern.

The evolution of the lowest P-wave IBG, S-wave IBG, and CBG with the increase of the pre-stretching is shown in Fig. 6e. Both the frequency and the width of the lowest S-wave IBG up-shift monotonically with the pre-stretch. Furthermore, with the upper boundary almost unchanged, the lower boundary of the first P-wave IBG shifts monotonically to lower frequencies as the pre-stretch increases. The dramatic frequency shift of the S-polarized branches in this P-wave IBG creates an intricate evolution of the CBGs. Nevertheless, the CBG generally gradually broadens and stabilizes with the increasing pre-stretching.

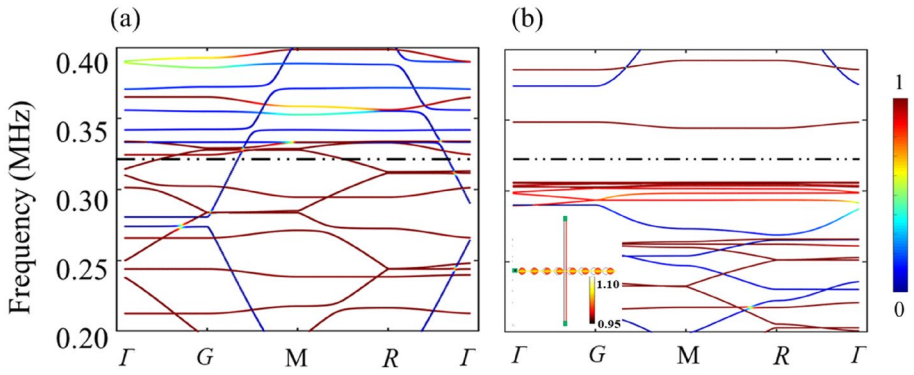

Fig. 7 Band structures of the 2D BCPL (unit cell and the corresponding Brillouin zone are shown in Fig. 2b, d. **a** and **b** are the band structures of the BCPL with the nominal strains $\varepsilon = 0$ and 0.1 in the x-direction. The color of the branches represents the dimensionless polarization. The deformation state and the corresponding distribution of the deformation gradient F_{11} of the 2D BCPL with pre-stretching are shown in the inset of (**b**)

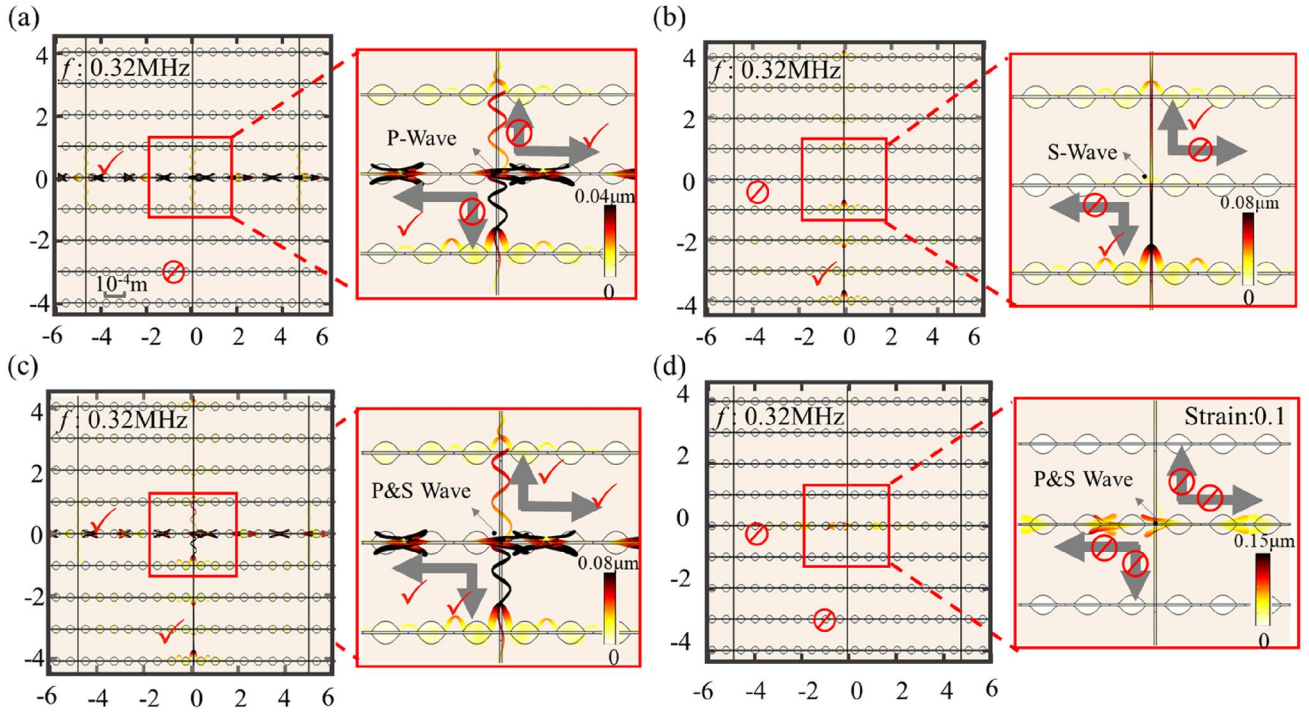

Fig. 8 Wavefield simulations of the 2D BCPL. **a**–**c** are the wavefields of the stress-free 2D BCPL with P-, S-, and coupled point sources applied in a node of the lattice. **d** is the same as **c** but the 2D BCPL is subject to pre-stretching $\varepsilon = 0.1$ in the x-direction

4.4 Elastic wave propagation in the 2D BCPL subject to pre-stretching

The influence of the pre-deformation of the 2D BCPL is shown in Fig. 7. For the primitive cell shown in Fig. 7b, we calculate the band structure in the undeformed and horizontally stretched (Fig. 7a, $\varepsilon = 0.1$) states, as shown in Fig. 8a, b.

For the undeformed 2D BCPL, many IBGs are exhibited in different intervals, allowing the design of directional transmission for specific elastic wave modes. For instance, the P-mode only exists in the ΓG and MR intervals at 0.32 MHz, whereas that of the S-counterpart is present in the other two intervals, as shown in Fig. 7a. The corresponding wavefield simulations for the P-, S-, and coupled point source applied at a node of the lattice are displayed in Fig. 8a–d, which not only demonstrates the directional transmission of the P-mode and S-mode in the horizontal (Fig. 8a) and vertical directions (Fig. 8b) but also indicates the mode separation for the coupled modes (Fig. 8c).

With the presence of the pre-stretch, two CBGs appear at [0.31, 0.34] MHz and [0.35, 0.37]MHz that are separated by a P-wave branch. In this case, the wavefield simulation demonstrates a contrasting difference to that shown in Fig. 8c. The coupled modes decay rapidly and cannot propagate in any direction in this type of horizontally elongated and prestressed structure, demonstrating the tunable wave-filtering capability of the 2D BCPL. Although recent work has systematically resolved Bloch wave propagation in a similar but simpler 2D soft lattice [22], fundamental mechanisms about the formation and evolution of band gaps under pre-stretching remain unclear due to the complexity of 2D BCPL. Related issues deserve systematic and independent study in the future.

5 Conclusion

In this paper, inspired by the morphology and material composition of spider capture silk, we present a lightweight 1D BCPL that possesses tunable bandgaps due to pre-stretching P-wave and S-wave IBGs and CBGs are observed in the band structure of the BCPL and verified by the transmission spectra. Through the analysis of the material composition, we demonstrate that the bandgap mid-frequencies and bandwidths can be effectively regulated by the shear modulus and the mass density of the bead. In addition, we give possible reasons for such careful design of the material parameters of the spider: the lowest possible density ensures a lightweight structure for the fabrication of the spider web, while compensating for the low shear modulus, which allows for a radial bandgap in

the web and thus contributes to the directional transmission of the vibration signal.

It is also shown that the finite pre-stretching significantly shifts the propagation modes distinctly and thus substantially broadens the bandgap. We also propose a 2D BCPL by imitating the local morphology of an orb-web and with the 1D BCPL as a component. Anisotropic bandgaps enable the structure to have directional transmission and mode separation of the elastic waves. The unidirectional finite pre-stretching produces a complete bandgap in the BCPL that permits features such as tunable wave-filtering.

The proposed 1D BCPL and 2D BCPL are structurally simple and easy to manufacture. Additionally, the parametric analysis provides essential guidance for the selection of materials. The BCPL's design will provide new opportunities to design and develop lightweight tunable elastic wave modulation devices, potential applications such as the vibration and noise reduction of the micro-electromechanical systems, directional propagation, and the wave-mode splitting of the elastic waves.

Acknowledgements This work was supported by the National Natural Science Foundation of China (Grant No. 11602294) and the 2115 Talent Development Program of the China Agricultural University.

Data availability All data generated and/or analyzed during this study are included in this article. The data are available from the corresponding author upon reasonable request.

Declarations

Conflict of interest The authors declare no competing interests.

References

1. M.S. Kushwaha, P. Halevi, L. Dobrzynski et al., Phys. Rev. Lett. **71**, 2022 (1993)
2. Y.S. Wang, W. Chen, B. Wu et al., Appl. Mech. Rev. **72**, 040801 (2020)
3. M.I. Hussein, M.J. Leamy, M. Ruzzene, Appl. Mech. Rev. **66**, 040802 (2014)
4. J.O. Vasseur, A.C. Hladky-Hennion, B. Djafari-Rouhani et al., J. Appl. Phys. **101**, 114904 (2007)
5. T.T. Wang, Y.F. Wang, Z.C. Deng et al., Mech. Syst. Sig. Process. **165**, 108392 (2022)
6. H. Lv, X. Tian, M.Y. Wang et al., Appl. Phys. Lett. **102**, 034103 (2013)
7. G. Hu, L. Tang, J. Liang et al., Smart Mater. Struct. **30**, 085025 (2021)
8. C.W. Muhammad, J. Lim, T.H. Li et al., Extreme Mech. Lett. **41**, 100994 (2020)
9. F. Casadei, L. Dozio, M. Ruzzene et al., J. Sound Vibrat. **329**, 3632 (2010)
10. Z. Liu, X. Zhang, Y. Mao et al., Science **289**, 1734 (2000)
11. C. Sugino, S. Leadenham, M. Ruzzene et al., J. Appl. Phys. **120**, 134501 (2016)
12. J. Wen, D. Yu, G. Wang et al., J. Phys. D: Appl. Phys. **41**, 135505 (2008)
13. A. Bergamini, M. Miniaci, T. Delpero et al., Nat Commun **10**, 4525 (2019)
14. Y.F. Zhang, D.L. Yu, J.H. Wen, Extreme Mech. Lett. **12**, 2 (2017)
15. P. Wang, F. Casadei, S. Shan et al., Phys Rev Lett **113**, 014301 (2014)
16. A.S. Phani, M.I. Hussein, *Dynamics of lattice materials* (Wiley, United Kingdom, 2017)
17. Y. Chen, T. Li, F. Scarpa et al., Phys. Rev. Appl. **7**, 024012 (2017)
18. P. Wang, F. Casadei, S.H. Kang et al., Phys. Rev. B **91**, 020103(R) (2015)
19. Y.F. Wang, Y.S. Wang, C. Zhang, J. Phys. D: Appl. Phys. **47**, 485102 (2014)
20. Y. Wei, X. Liu, G. Hu, Mater. Des. **210**, 110031 (2021)
21. Y. Wang, B. Yousefzadeh, H. Chen et al., Phys Rev Lett **121**, 194301 (2018)
22. S. Zhao, T. Feng, H. Zhang et al., Mech. Syst. Sig. Process. **181**, 109487 (2022)
23. Y.L. Huang, N. Gao, W.Q. Chen et al., Acta Mech. Solida Sin. **31**, 51 (2018)
24. K. Bertoldi, M.C. Boyce, Phys. Rev. B **78**, 184107 (2008)
25. E.G. Barnwell, W.J. Parnell, I.D. Abrahams, Extreme Mech. Lett. **12**, 23 (2017)
26. P. Wang, J.M. Shim, K. Bertoldi, Phys. Rev. B **88**, 014304 (2013)
27. R.K. Pal, J. Rimoli, M. Ruzzene, Smart Mater. Struct. **25**, 054010 (2016)
28. Y. Liu, Z. Chang, X.Q. Feng, Extreme Mech. Lett. **11**, 37 (2017)
29. W.M. Masters, Behav. Ecol. Sociobiol. **15**, 207 (1984)
30. M. Denny, J. Exp. Biol. **65**, 483 (1976)
31. B. Mortimer, A. Soler, C.R. Siviour et al., J. R. Soc. Interface **13**, 20160341 (2016)
32. Y. Guo, Z. Chang, B. Li et al., Appl. Phys. Lett. **113**, 103701 (2018)
33. M. Miniaci, A. Krushynska, A.B. Movchan et al., Appl. Phys. Lett. **109**, 071905 (2016)
34. Q. Zhang, X. Yang, P. Li et al., Prog. Mater Sci. **74**, 332 (2015)
35. H.K. Zhang, X.Q. Feng, Extreme Mech. Lett. **43**, 101166 (2021)
36. F. Ma, J.H. Wu, M. Huang et al., Appl. Phys. Lett. **105**, 213702 (2014)
37. E. Wirth, F.G. Barth, J. Comp, Physiol A. **171**, 359 (1992)
38. J. Zhou, J. Lai, G. Menda et al., Proc Natl Acad Sci U S A **119**, e2122789119 (2022)
39. M.A. Landolfa, F.G. Barth, J Comp Physiol A **179**, 493 (1996)
40. S.D. Stellwagen, B.D. Opell, K.G. Short, J. Exp. Biol. **217**, 1563 (2014)
41. Y. Guo, Z. Chang, H.Y. Guo et al., J. R. Soc. Interface **15**, 20170894 (2018)
42. R. Foelix, *Biology of Spiders* (Oxford University Press, New York, 2010)
43. J.L. Yarger, B.R. Cherry, A. van der Vaart, Nat. Rev. Mater. **3**, 1 (2018)
44. Y.J. Qian, Q.D. Cui, X.D. Yang et al., Int. J. Mech. Sci. **168**, 321 (2020)
45. X. Qi, T. Li, J. Zhang et al., Appl. Phys. A. **11**, 124 (2018)
46. L. Lei, L. Miao, H. Zheng et al., Appl. Phys. A. **22**, 128 (2022)
47. J.C. Guo, Z. Zhang, Appl. Phys. A. **2**, 128 (2022)
48. R.W. Ogden, *Non-linear elastic deformations* (Courier Corporation, New York, 1997)
49. G. Bordiga, L. Cabras, A. Piccolroaz et al., J. Mech. Phys. Solids **146**, 104198 (2021)
50. S. Zhao, Z. Chang, Int. J. Solids Struct. **233**, 111208 (2021)
51. K.J. Koski, P. Akhenblit, K. McKiernan et al., Nat. Mater. **12**, 262 (2013)
52. M.F. Ashby. *The CES Edupack database of natural and man-made materials*, (Cambridge University and Granta Design, Cambridge, UK, 2008)
53. H. Zhang, X. Guo, J. Wu et al., Sci. Adv. **4**, 8535 (2018)

54. L.L. Chen, Z. Chang, T.Y. Qin, Int. J. Solids Struct. **126**, 1 (2017)
55. M.C. Boyce, Rubber Chem. Technol. **69**, 781 (1996)
56. W. Nafo, A. Al-Mayah, Exp. Mech. **59**, 1047 (2019)
57. J.C. Simo, K.S. Pister, Comput. Methods Appl. Mech. Eng. **46**, 201 (1984)
58. L. Meng, X. Yang, E. Salcedo et al., J. Mater. Eng. Perform. **29**, 2597 (2020)
59. H. Berjamin, R. De Pascalis, Int. J. Solids Struct. **241**, 111529 (2021)
60. Y. Achaoui, A. Khelif, S. Benchabane et al., J. Phys. D: Appl. Phys. **43**, 185401 (2010)